



# In situ hard X-ray transmission microscopy for material science

Ken Vidar Falch<sup>1</sup>, Daniele Casari<sup>1</sup>, Marco Di Michiel<sup>2</sup>, Carsten Detlefs<sup>2</sup>, Anatoly Snigireva<sup>3</sup>, Irina Snigireva<sup>2</sup>, Veijo Honkimäki<sup>2</sup>, and Ragnvald H. Mathiesen<sup>1,\*</sup>

<sup>1</sup>Department of Physics, Norwegian University of Science and Technology, Høgskoleringen 1, 7491 Trondheim, Norway

<sup>2</sup>European Synchrotron Radiation Facility, 71 Avenue Des Martyrs, 38000 Grenoble, France

<sup>3</sup>Immanuel Kant Baltic Federal University, Kaliningrad, Russia 238300

**Received:** 4 November 2016

**Accepted:** 24 November 2016

**Published online:**

2 December 2016

© Springer Science+Business Media New York 2016

## ABSTRACT

Hard X-ray transmission microscopy based on refractive X-ray optics can be employed as a tool in material science to investigate buried-in microstructures in two or three dimensions with spatial resolution approaching 100 nm. Switching from monochromatic to radiation with a broader bandwidth, frame rates down to a few milliseconds can be realized, opening new possibilities for in situ studies of microstructure evolution and response to external fields at spatiotemporal resolutions that go well beyond previous benchmarks, demonstrated by ~200 nm resolution tomograms of eutectic microstructures acquired in less than 2 s. The microscope can also be operated in Zernike phase contrast mode, which expands the range of possible applications to cases which otherwise would produce only very faint contrast. A few possible application areas for the microscope are illustrated by a selection of material science test cases.

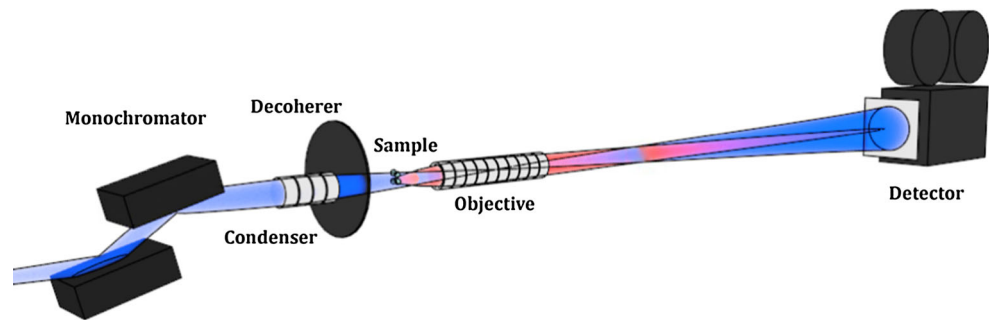
## Introduction

Compared to electron- or visible-light microscopy, an X-ray-based alternative would have enhanced sample penetration depth and would allow for observations of the internal structures of otherwise opaque samples. Many samples, however, would remain opaque at photon energies well into the softer part of the X-ray regime. When this is the case, harder X-rays must be employed to increase the penetrating power. Herein, hard X-rays refer to photon energies above 15 keV, considered outside the typical operating range for conventional diffractive X-ray optics.

At present, non-magnified projection radiography at synchrotrons can reach spatial resolutions down to ~0.7 μm. For in situ studies, extreme temporal resolutions can be reached, with exposure times down to the ~10 ns range, and frame rates up to 1.4 MHz [1–3]. However, the high temporal resolution comes at the expense of both field of view and spatial resolution which in these setups is limited to several tens of microns. In high-resolution X-ray imaging detectors, it is a common practice to use indirect detection, i.e. to place a light microscope between a CCD or CMOS pixel array and a scintillator crystal that converts X-rays into visible light. The effective

Address correspondence to E-mail: Ragnvald.Mathiesen@ntnu.no

**Figure 1** Schematic illustration of the hard X-ray transmission microscopy setup.



pixel size is determined by the physical CCD/CMOS pixel size, the optical magnification and spatial resolution of the visible-light microscope, and the thickness of the scintillator crystal. Current limits for such setups may yield temporal resolution of  $\sim 1$  ms in combination with an effective pixel size of  $\sim 0.5$   $\mu\text{m}$  over a Field of View (FoV) of  $\sim 1$   $\text{mm}^2$  [4]. Geometrically magnified radiography based on micro-focus home laboratory X-ray sources, on the contrary, is ultimately limited in spatial resolution by the source size to 1–2  $\mu\text{m}$  and to temporal resolutions  $>0.2$  s [5, 6].

The pixel size, source size, and time resolution limitations can all be lifted by using synchrotron radiation with X-ray optical elements to create magnified and focused X-ray images, i.e. by using X-ray microscopy. The magnification of the X-ray image further reduces the effective pixel size, and the fact that the image is focused, as opposed to projected, eliminates any adverse effects of the source size. In fact, increasing the source size will usually have a positive effect on the spatial resolution [7].

For in situ applications, a compromise must be struck between spatial and temporal resolution. A good temporal resolution has merit on its own. Furthermore in studies of non-static samples, temporal and spatial resolution are coupled due to blurring of contrast objects in motion relative to the detector system during exposure, i.e. so-called motion blurring. Thus, it is desirable to increase the frame rate whenever possible, provided that the exposure remains adequate to obtain a reasonable signal-to-noise ratio. The high efficiency of compound refractive lenses (CRLs) [8] makes them a suitable choice for in situ hard X-ray transmission microscopy (HXTM). Other reasonable choices are reflective optics [9], and multilayer Laue lenses [10]. X-ray microscopy based on Fresnel zone plates (FZPs) has for a long time been used to study a wide range of

samples [11–13]. However, FZPs are used primarily at energies below 12–15 keV due to their low efficiency in the hard X-ray regime [14]. While FZPs can achieve spatial resolution as low as 15 nm on static samples [15], they are currently not suitable for in situ applications with hard X-rays.

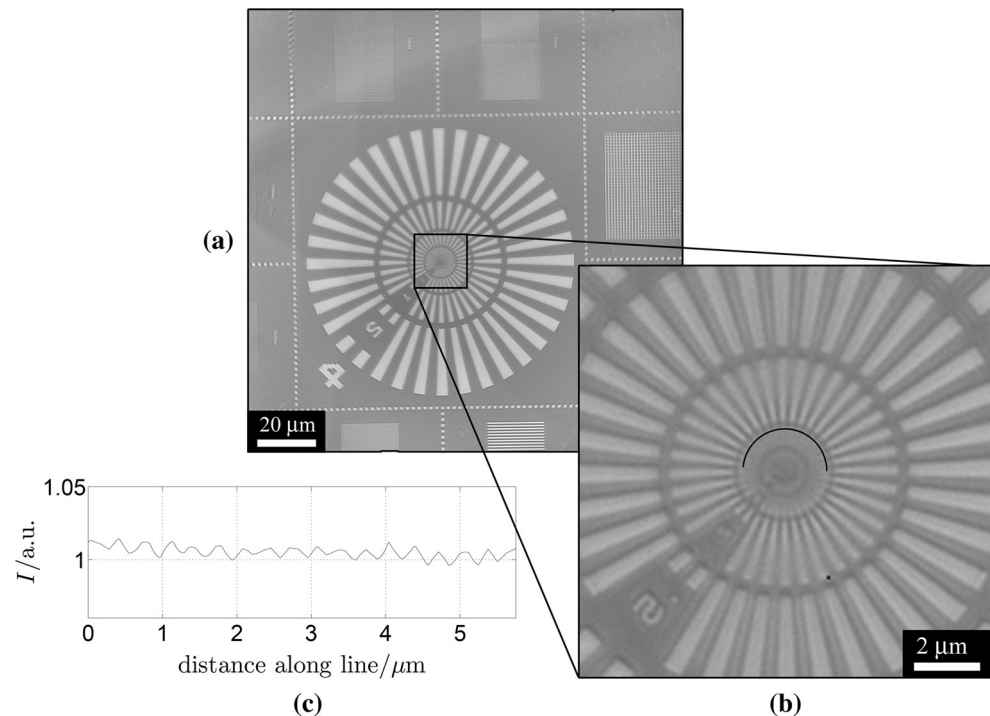
Using CRL-based HXTM, both 2D and 3D images can be produced with spatial resolution down to 100–200 nm [16], while maintaining frame rates comparable to parallel beam performance,  $\sim 1$  kHz.

## Method

A schematic drawing of a CRL-based full field microscope is illustrated in Fig. 1. The monochromator is used to filter out photons that are not at the desired energy, increasing the spatial resolution at the cost of photon flux, which in turn affects the temporal resolution. In this setup, the illuminating beam goes through the condenser, illuminates the sample, goes through the objective lens, and hits the detector. The physical pixel size of the CCD/CMOS camera is typically 5–15  $\mu\text{m}$  but the visible-light microscope can magnify the image of the scintillator by a factor of  $\sim 10$ –20. These are the standard working principles for high-resolution X-ray detectors used for imaging at synchrotron sources [6, 17, 18].

The inclusion of the X-ray lens further magnifies the image, making the effective pixel size even smaller. The X-ray magnification typically lies in the 5–100 range [16, 19] but is not strictly limited at either bound. With the extra magnification from X-ray optics, the maximum spatial resolution is no longer limited by the detector pixel size, but by the X-ray optical components. The main factors that influence the spatial resolution are the numerical aperture and aberrations of the objective CRL. Of secondary importance, but by no means negligible, are the properties of the illuminating

**Figure 2** a Image of a Siemens star resolution test object, with its inner structures enlarged in (b). Finest resolved line is 165 nm wide, corresponding to 3.0 lp/ $\mu\text{m}$ . c Intensity profile sampled from the *black arc* in (b).



beam. The use of a condenser lens and a beam decoherer can greatly improve the image quality. A condenser lens increases the intensity of the illumination, and can also be thought of as increasing the effective numerical aperture, which improves spatial resolution. A decoherer usually comprises a disc, inserted in the beam somewhere upstream of the sample, that destroys the spatial coherence of the incident X-rays by scattering. The disc is spun to average out structure in the scattering, providing an even illumination. The most notable effect of the decoherer is the removal of speckles stemming from imperfections of beam line optics such as Be-windows, multilayer mirrors, and the condensing optics.

An example of the capabilities of the CRL HXTM is given in Fig. 2, which shows an image of a Siemens star resolution test object [20]. The resolution was  $\sim 150$  nm over a  $\sim 150 \mu\text{m} \times 150 \mu\text{m}$  field of view, using 17 keV photon energy. It is worth mentioning that a recent development [21] could make Multilayer Laue Lenses a good option for HXTM. With Multilayer Laue Lenses, resolution in the 15–50 nm range is possible [22–24].

### Monochromatic versus pink beam illumination

In most X-ray microscopy experiments, the incident beam is energy filtered by a Si-111 double crystal

monochromator to a relative bandwidth  $\Delta E/E \sim 10^{-4}$ , where  $E$  is the peak energy and  $\Delta E$  is the width of the peak (full width at half maximum). For HXTM, synchrotron undulator sources are the preferred alternative over bending magnet or wiggler sources, due to the higher brightness of the undulator. The energy spectrum emitted from an undulator is concentrated in harmonic peaks [25], typically with  $\Delta E/E \sim 10^{-2}$ . Thus, when a monochromator is employed, only a narrow part of one of the harmonic peaks is used to illuminate the sample. Approximately two orders of magnitude in flux can be gained by using the full undulator harmonic peak, i.e. so-called pink beam illumination, allowing temporal resolution down to the ms range. While monochromatization is beneficial for the spatial resolution of static samples, it is often the temporal resolution that ultimately determines the spatial resolution for in situ experiments.

Traditional chromatic correction schemes used with visible-light optics, that rely on combining positive and negative lenses of different materials [26, 27], are not suitable for X-ray lenses, but it is possible to limit chromatic aberrations by using short focal lengths and focusing the illumination at a locus inside the objective [28]. A potential benefit of chromatic aberrations is the artificially increased depth of field due to the ambiguity of the imaging condition in

a chromatic beam. Forthcoming improvements to synchrotron storage rings, i.e. so-called new generation low emittance storage rings [29, 30], are likely to increase the temporal resolution for pink beam, as well as monochromatic X-ray microscopy due to the expected 10–100 times increased brilliance [29]. Furthermore, the bandwidth of undulator peaks is also expected to decrease by one order of magnitude, further reducing chromatic aberrations.

### Tomography

With X-ray energies sufficient to penetrate bulky samples, a series of 2D projection images taken for different sample orientations about a fixed rotation axis can be used for 3D sample reconstructions in the form of a tomogram. Tomographic imaging is frequently used with X-ray microscopes [31, 32]. Typically, 500–2000 radiography projections are needed to make a complete high-resolution tomogram, with acquisition times corresponding to the accumulated frame exposures. Although this poses a challenge for many in situ experiments, it will be shown here that pink beam illumination can be used to record tomograms in  $\sim 1$  s.

### Zernike phase contrast

In the standard implementation of HXTM, the main contrast mechanism is absorption. Contrast becomes weaker with increasing photon energy. If high energy photons are needed to penetrate the sample, or to avoid radiation damage or heating of the sample, then the absorption contrast will likely be weak. Furthermore, some samples produce only weak absorption contrast even with fairly soft X-rays. When this is the case, it is beneficial to turn to phase contrast rather than absorption contrast. In general, phase contrast is stronger than absorption contrast with X-rays [25].

Zernike phase contrast (ZPC) is a microscopy technique that produces phase contrast by converting phase modulations in the image into detectable amplitude modulations [33]. This is different from propagation-based phase contrast, which relies on near-field interference fringes around sample features [34–36]. Since ZPC is not propagation based, phase contrast can be obtained while keeping a sharp image, without numerical phase retrieval.

ZPC can be introduced into a standard microscope with only minor modifications. A phase plate of appropriate dimensions must be inserted into the beam somewhere downstream of the sample, preferably near or inside the objective, and the illumination must be focused at the phase plate. The X-rays that are scattered from the sample will be distributed over a larger beam cross section. Therefore, when the phase plate has the appropriate size, it will selectively phase shift the background illumination by  $\pi/2$  with respect to the scattered X-rays. This phase shift causes the phase modulation, rather than the absorption modulation, to interfere with the background to form the image. It is possible to fix the phase plate inside the objective, eliminating the need for an extra set of motors to align the phase plate [19]. Selection of a suitable material and optimization of the phase plate diameter and thickness depend both on the X-ray photon energy and on the exact X-ray optical configuration chosen, like CRL physical aperture, focal distance and focal spot size, and are therefore highly case specific. Further details on how to assign the appropriate phase plate parameters can be found elsewhere [19].

## Results and discussion

### Radiography with monochromatic illumination

One potential application area for HXTM is in situ studies of eutectic phase transformations in metallic alloys. In the Al–Si irregular eutectic, a faceted Si component tends to lead the eutectic transformation since it generally requires a higher growth undercooling than the non-faceted Al component to be able to branch effectively and expand into a 3D network. The introduction of certain elements, such as Na, Sr or Ca, can alter both the nucleation conditions and the branching ability of the Si crystals at the growth front, leading to a remarkable refinement of the eutectic microstructure [37–41]. HXTM in situ microscopy may contribute to advance the understanding of such nucleation and growth mechanisms. The images in shown Fig. 3 were obtained using HXTM with 17 keV monochromatic radiation, and captures the nucleation and growth of a faceted Si crystal in a slightly hypo-eutectic Al–16.4Cu–7.1Si (all compositions are in wt%, unless otherwise indicated)

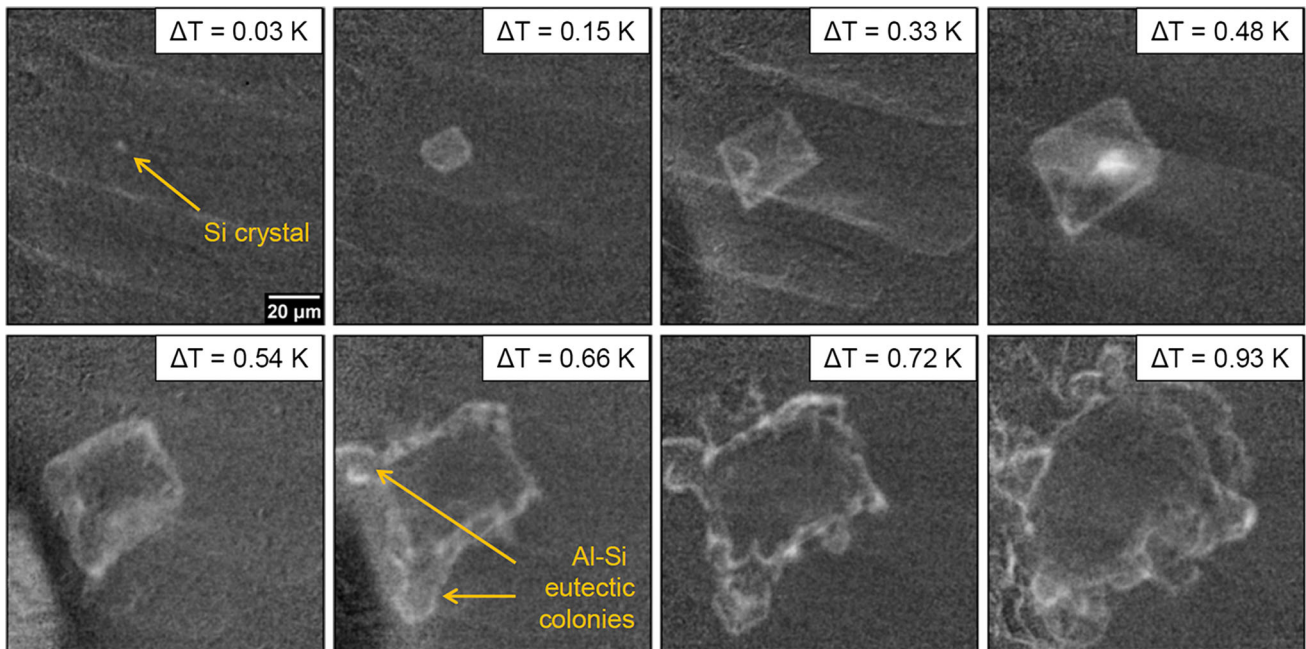


**Figure 3** Sr-modified irregular eutectic microstructure formation in near-isothermal solidification of Al-16.4Cu-7.1Si alloy with 5 ppm P and 100 ppm Sr added.  $\Delta T$  values given in the *upper*

*right* of each image are relative to the frame at which the Si crystal is first observed in the field of view. The cooling rate was 0.1 K/s.

with 5 ppm P and 100 ppm Sr added to provide nucleation sites for Si and to yield eutectic modification, respectively. The resolution offered by HXTM allows for unambiguous identification of the particle as a Si crystal at an early growth stage based on its octahedral growth morphology [42, 43]. Differently from previous studies with conventional synchrotron radiation imaging [44], the spatiotemporal resolution achieved by HXTM makes it possible to study in detail how branching evolves from the primary Si-crystal. After nucleation and a few seconds of Si crystal growth, instabilities and structures are observed to evolve starting from two vertices and then from the edges of the crystal, which act as substrates to formation of Al-Si eutectic colonies. In this example,  $10\times$  magnifications were employed both for the visible-light camera and the X-ray microscope yielding an effective pixel size of 125 nm. The exposure time was 0.3 s.

### Radiography with pink beam illumination

Regular eutectics have been thoroughly investigated over the last fifty years. For binary systems, there are well-established models available to link the eutectic pattern formation, planar interface stability and

growth, and further insight into the limits of stability is continuously driven forward by in situ experiments and numerical simulations [6, 45–52]. For multicomponent systems, however, and for systems processed under conditions that fall outside the range where the existing framework can be applied, it is of both fundamental and practical interest to understand the exact conditions under which regular eutectic patterns are stabilized, destabilized and altered [53–58]. For instance, planar-to-cellular and planar-to-dendritic eutectic morphology transitions have been demonstrated in situ with parallel beam synchrotron radiography in the Al–Cu–Ag ternary system [54]. However, while the spatiotemporal resolution was adequate to detect the eutectic morphology transitions at a mesoscopic scale, it did not allow for a simultaneous tracking of the detailed and dynamic changes in the eutectic lamella patterns during morphological transitions.

Figures 4 and 5 show selected frames from directional solidification experiments performed on a binary Al–33Cu alloy and a ternary Al–33Cu–2.8Ag alloy, respectively. In both cases, the solidification direction is downwards, parallel with gravity. For the Al–33Cu binary system, a Al–Al<sub>2</sub>Cu eutectic quasi-planar front was established in the FoV (Fig. 4) under

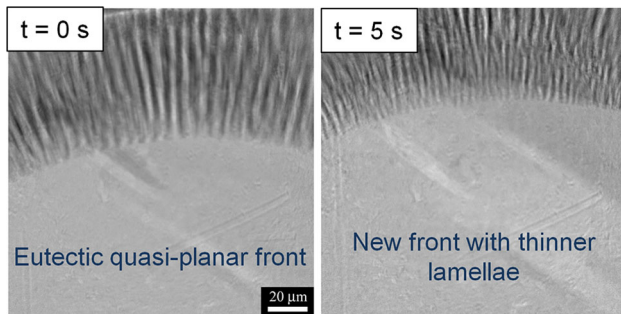


**Figure 4** Decreased lamella spacing of Al-Cu regular eutectics during accelerated directional solidification. The solidification parameters were set as follows: thermal gradient 65 K/mm, cooling rate 0.05 K/s, and in the latter parts of the sequence: pulling speed 10  $\mu\text{m/s}$ . Times given in the *upper left* of each image are relative to the first frame of the figure.

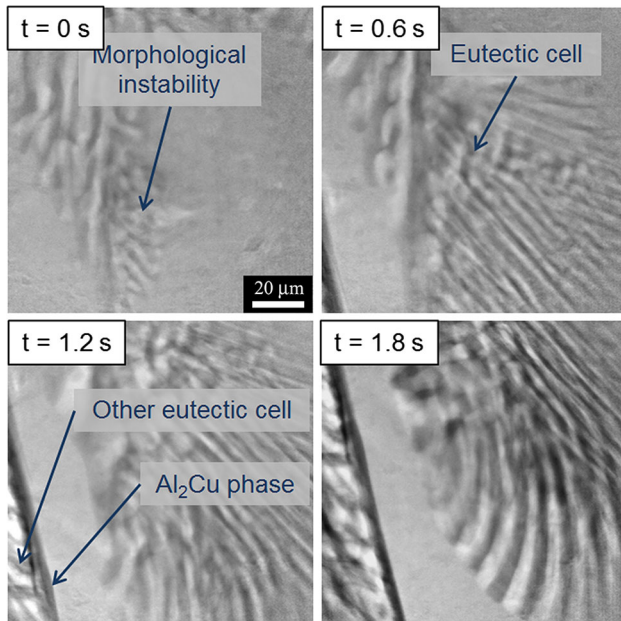


**Figure 5** Representative radiograms taken during cellular regular eutectic growth in directional solidification of Al-33Cu-2.8Ag alloy. The solidification parameters were set as follows: thermal gradient 25 K/mm and pulling speed 2  $\mu\text{m/s}$ . Times given in the *upper left* of each image are relative to the first frame of the figure.

constant temperature gradient of 65 K/mm and cooling rate of 0.05 K/s, imposed to both furnace compartments. When semi-steady growth had established, the growth front and eutectic pattern were destabilized increasing the cooling rate by introducing a pulling of the sample at a constant speed of 10  $\mu\text{m/s}$  into the upper cold furnace compartment. In accordance with theory, this caused a

refinement of the growth pattern by the formation of new lamellae, leading to a decrease in the lamellar spacing from  $\sim 6$  to  $\sim 3$   $\mu\text{m}$ . The dynamic evolution of the microstructure could be easily monitored due to the high spatial and temporal resolution achieved with HXTM and pink beam illumination.

In this experiment, the exposure time was 20 ms, and the effective pixel size was 125 nm. The magnification of the visible-light optics was 10 while the X-ray magnification was 8. Similarly to the monochromatic experiment presented in the previous subsection, the X-ray energy was 17 keV. A relative bandwidth of 1.4% (full width at half maximum) was used. Although this experiment was not identical to the monochromatic experiment presented above in terms of sample contrast and image quality, pink beam illumination improved the time resolution by at least an order of magnitude. Furthermore, the average photon count per pixel was more than 5–10 times larger in the pink beam experiment. Note that, the real gain in time resolution is highly situational, as it depends on bandwidth, the spatial coherence of the illumination, and the required resolution. The benefits of high spatiotemporal resolution are particularly evident for the case of the ternary Al-33Cu-2.8Ag alloy (Fig. 5), in which the changes in eutectic lamella patterns associated with morphological transitions occur very rapidly.

For the in situ radiography demonstrations shown in Figs. 3, 4, and 5, a gradient furnace of the Bridgman-type was applied, with two independently controlled heaters separated by an adiabatic zone of 4 mm, and with the X-ray camera field of view situated in the centre of the adiabatic zone. Although this furnace has been used extensively and successfully in other in situ solidification studies [5, 6], a custom built furnace with an adjustable adiabatic zone would be preferable for future studies. The alloys used in these studies were prepared from high purity master alloys, and cast in a bottom-chilled Cu mould. Sample material was taken from the central region of the castings, grinded and polished down to  $\sim 190$   $\mu\text{m}$  thin sheets with lateral dimension  $50 \times 5$   $\text{mm}^2$ .

## Tomography

Investigations of phenomena associated with microstructure formation and pattern selection during solidification would greatly benefit from extending in situ observations to three dimensions. By

reducing the minimum exposure time and consequently the total acquisition time needed to record a tomogram, pink beam illumination enables meaningful 3D studies of solidification microstructures. Figure 6 shows a slice of a reconstructed tomogram of a solidified Al–Al<sub>2</sub>Cu eutectic microstructure. The tomogram was constructed from 900 projections, each recorded with 2 ms exposure time, making the total acquisition time 1.8 s, and spanning a volume of  $\sim 200 \times 200 \times 200 \mu\text{m}^3$ . The lamella spacing is observed to vary markedly across the field of view, where the smallest lamella half-period measured was 270 nm. The magnification of the X-ray image was 8 while the magnification of the visible-light optics was 10.

Another interesting application of HXTM is tomography investigations of colloidal crystals. Studies of colloids are of interest to several research fields such as soft matter [59], biology [60], photonic crystals [61], and fundamental solidification science [62], to mention some. Many studies of colloids are based, or partially based, on visible-light confocal microscopy [63–65]. The improved resolution of HXTM makes it possible to directly observe systems with sub-micron-sized particles. Furthermore, HXTM is capable of rapid 3D imaging of colloidal crystal structures, which could allow for in situ studies of

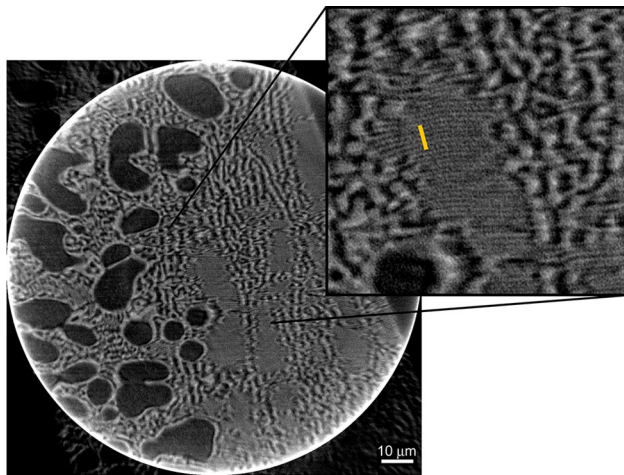


**Figure 6** Reconstructed tomogram slice of Al–Al<sub>2</sub>Cu eutectic microstructure recorded using 17 keV photon energy. Large dark pockets are  $\alpha$ -Al primary dendrites, while dark and bright areas inside the eutectic are the Al phase and the Al<sub>2</sub>Cu phase, respectively. The smallest lamellae half-period found was  $\sim 270$  nm. The orange line in the zoomed view indicates where the lamellae were measured, averaging over 5 periods. The pixel size is 125 nm.

self-assembly in several different experimental conditions, and under the application of external fields such as temperature, pressure or electromagnetic fields for charged or paramagnetic particle systems. However, it should be mentioned that controlling temperatures under pink beam illumination poses an experimental challenge due to a local beam-induced heating.

Figure 7 demonstrates the possibility of recording tomograms of colloidal crystals made of 1.5- $\mu\text{m}$ -diameter silica spheres using HXTM. The images were recorded with 0.3% energy bandwidth. In this case, both the magnification of the X-ray image and the visible-light optics between the scintillator and the camera were 10. The effective pixel size was 110 nm and the field of view was  $\sim 100 \mu\text{m} \times \sim 100 \mu\text{m}$ . The tomogram was reconstructed from 900 projections, each acquired with 30-ms exposure time, making the total acquisition time 27 s, which is relatively long compared to the acquisition time used to obtain the tomogram in Fig. 6. The relatively slow acquisition time for the colloid tomogram was due to particular circumstances during the experiment that caused a severe flux reduction of the incident beam. It is reasonable to expect that the tomogram could be acquired at a similar time scale as in Fig. 6 given the same experimental conditions.

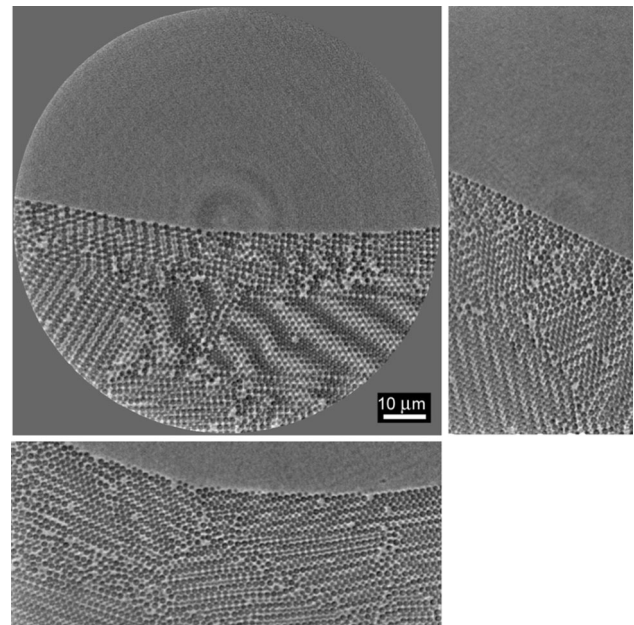


**Figure 7** Orthogonal slices from tomographic reconstruction of colloidal crystal grains made of 1.5- $\mu\text{m}$ -diameter SiC spheres. The pixel size was 110 nm. The tomogram was recorded using 20 keV photon energy.

An overview of the current capabilities of other imaging techniques suitable for imaging colloid particles can be found in a recently published paper [66]. Even with experimental difficulties, the acquisition time made possible by HXTM is a significant improvement over other methods, with the exception of the stimulated emission depletion technique which has reported imaging with 50-ms exposure time [67]. The high penetrating power of hard X-rays and the large depth of field due to the short wavelength and chromaticity makes HXTM capable of handling the  $\sim 1$  mm sample thickness without problems.

### Zernike phase contrast

As an illustration of the effect of using ZPC with HXTM, still images of Al–Si microstructure using both ZPC and non-ZPC in a monochromatic beam are shown for comparison in Fig. 8. For adequate transmission through 100–200 micrometers of an Al–Si alloy, hard X-rays with photon energy above  $\sim 10$  keV are needed. At such energies, however, the absorption contrast between the two elements is very weak, as their photo-electric absorption edges lie below 2 keV, making it difficult to distinguish between, e.g. the  $\alpha$ -Al primary phase and the Al–Si eutectic phase. Employing ZPC improves the contrast remarkably. The images were recorded with an X-ray magnification of 3, and a visible-light magnification of 20, resulting in a pixel size of 240 nm.

Concerns have been raised regarding the ability of HXTM to image weakly absorbing particles [67]. With ZPC, however, imaging of single small organic particles, like e.g. polystyrene, is indeed possible. Figure 9 shows images of 2- $\mu$ m-diameter polystyrene spheres on a membrane. The experimental setup was

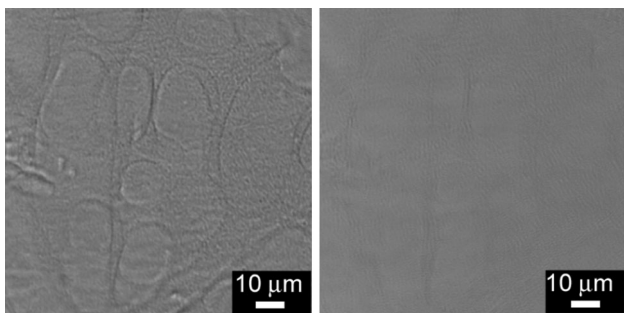


**Figure 8** Comparison of image contrast in a Al–Si alloy sample with and without ZPC on the *left* and *right*, respectively. The photon energy was 17 keV, and the pixel size was 240 nm.

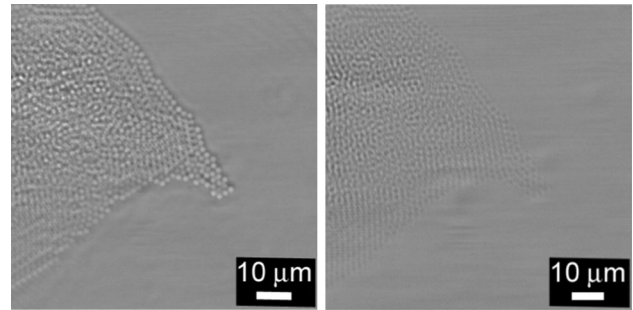


**Figure 9** Comparison of image contrast 2- $\mu$ m-diameter polystyrene spheres with and without ZPC on the *left* and on the *right*, respectively. The photon energy was 17 keV, and the pixel size was 240 nm.

the same as the one used for acquiring the images shown in Fig. 8. Although absorption in the polystyrene is negligible, the spheres are visible, even without ZPC, due to scattering contrast. This contrast, however, is much weaker compared to the phase contrast produced by ZPC. This point is well illustrated at the edges of the colloidal cluster, where particles remain clearly distinguishable, even as the sample becomes a monolayer. It is also worth noting that even in cases where the absorption contrast is reasonable, it might be worth using ZPC to improve the signal-to-noise ratio, to further reduce the acquisition time.

### Conclusion

In situ studies of microstructure evolution or changes in response to external fields in materials can be extended to resolutions beyond the current limits by the new hard X-ray transmission microscopy being developed at the ESRF. Using compound refractive X-ray optics, the microscope can be operated both in monochromatic and non-monochromatic modes, the latter by applying a special illumination scheme that works effectively to reduce chromatic aberrations. The non-monochromatic mode provides to orders of magnitude increase of the brilliance in the sample position, which opens for X-ray tomography acquisition on the scale of 1–2 s, with spatial resolutions below 200 nm, while radiography with similar spatial resolution can be acquired at millisecond frame rates. Potential application areas of fast 2D and 3D microscopy have been demonstrated with a few selected test cases, comprising regular and irregular eutectic solidification microstructure formation in different



Al-based alloys, and self-assembly of colloidal crystal systems composed of different polymer particles with diameters in the micrometer range. Operation of the microscope in Zernike phase contrast extends the range of possible applications to samples that otherwise would produce only faint contrast.

## Acknowledgements

The authors would like to acknowledge the Norwegian Research Council (Project Grant No. 218404/F50) and the European Synchrotron Radiation Facility for their support to this research project.

## Compliance with ethical standards

**Conflict of interest** The authors declare that they have no conflict of interest.

## References

- [1] Rack A, Scheel M, Hardy L, Curfs C, Bonnin A, Reichert H (2014) Exploiting coherence for real-time studies by single-bunch imaging. *J Synchrotron Radiat* 21:815–818. doi:10.1107/S1600577514005852
- [2] Rack A, Scheel M, Danilewsky AN (2016) Real-time direct and diffraction X-ray imaging of irregular silicon wafer breakage. *Iucrj* 3:108–114. doi:10.1107/S205225251502271x
- [3] Pelliccia D, Rack A, Scheel M, Cantelli V, Paganin DM (2016) Experimental X-ray ghost imaging. *Phys Rev Lett* 117(11):113902. doi:10.1103/PhysRevLett.117.113902
- [4] Douissard PA, Cecilia A, Rochet X, Chapel X, Martin T, van de Kamp T, Helfen L, Baumbach T, Luquot L, Xiao X, Meinhardt J, Rack A (2012) A versatile indirect detector design for hard X-ray microimaging. *J Instrum*. doi:10.1088/1748-0221/7/09/P09016
- [5] Nguyen-Thi H, Reinhart G, Salloum-Abou-Jaoude G, Browne DJ, Murphy AG, Houlitz Y, Li J, Voss D, Verga A, Mathiesen RH, Zimmermann G (2014) XRMON-GF experiments devoted to the in situ X-ray radiographic observation of growth process in microgravity conditions. *Microgravity Sci Technol* 26(1):37–50. doi:10.1007/s12217-014-9370-4
- [6] Murphy AG, Browne DJ, Mirihanage WU, Mathiesen RH (2013) Combined in situ X-ray radiographic observations and post-solidification metallographic characterisation of eutectic transformations in Al-Cu alloy systems. *Acta Mater* 61(12):4559–4571. doi:10.1016/j.actamat.2013.04.024
- [7] Hopkins HH, Barham PM (1950) The Influence of the Condenser on Microscopic Resolution. *P Phys Soc Lond B* 63(370):737–744. doi:10.1088/0370-1301/63/10/301
- [8] Schroer CG, Kuhlmann M, Lengeler B, Gunzler TF, Kurapova O, Benner B, Rau C, Simionovici AS, Snigirev AA, Snigireva I (2002) Beryllium parabolic refractive X-ray lenses. *Des Microfabr of Novel X-ray Opt* 4783:10–18. doi:10.1117/12.451013
- [9] Matsuyama S, Emi Y, Kino H, Kohmura Y, Yabashi M, Ishikawa T, Yamauchi K (2015) Achromatic and high-resolution full-field X-ray microscopy based on total-reflection mirrors. *Opt Express* 23(8):9746–9752. doi:10.1364/Oe.23.009746
- [10] Koyama T, Takano H, Konishi S, Tsuji T, Takenaka H, Ichimaru S, Ohchi T, Kagoshima Y (2012) Circular multi-layer zone plate for high-energy x-ray nano-imaging. *Rev Sci Instrum* 83(1):013705. doi:10.1063/1.3676165
- [11] Baez AV (1961) Fresnel zone plate for optical image formation using extreme ultraviolet and soft X radiation. *J Opt Soc Am* 51(4):405–412
- [12] Kirz J, Rarback H (1985) Soft-X-ray microscopes. *Rev Sci Instrum* 56(1):1–13. doi:10.1063/1.1138464
- [13] Jacobsen C (1999) Soft x-ray microscopy. *Trends Cell Biol* 9(2):44–47. doi:10.1016/S0962-8924(98)01424-X
- [14] Wu SR, Hwu Y, Margaritondo G (2012) Hard-X-ray Zone Plates: Recent Progress. *Materials* 5(10):1752–1773. doi:10.3390/ma5101752
- [15] Chao W, Kim J, Rekawa S, Fischer P, Anderson EH (2009) Demonstration of 12 nm resolution Fresnel Zone plate lens based soft X-ray microscopy. *Opt Express* 17(20):17669–17677. doi:10.1364/Oe.17.017669
- [16] Snigireva I, Vaughan GBM, Snigirev A (2011) High-energy nanoscale-resolution X-ray microscopy based on refractive optics on a long beamline. 10th International Conference on X-Ray Microscopy 1365:188–191
- [17] Mathiesen RH, Arnberg L, Nguyen-Thi H, Billia B (2012) In situ X-ray video microscopy as a tool in solidification science. *Jom-Us* 64(1):76–82. doi:10.1007/s11837-011-0213-0
- [18] Zabler S, Rueda A, Rack A, Rieseheimer H, Zaslansky P, Manke I, Garcia-Moreno F, Banhart J (2007) Coarsening of grain-refined semi-solid Al-Ge32 alloy: X-ray microtomography and in situ radiography. *Acta Mater* 55(15):5045–5055. doi:10.1016/j.actamat.2007.05.028
- [19] Falch KV, Lyubomirskij M, Casari D, Detlefs C, Snigirev A, Snigireva I, Di Michiel M, Mathiesen R (2016) Zernike phase contrast in high-energy X-ray transmission microscopy based on refractive optics. *Ultramicroscopy* under review.
- [20] X-ray chart NTT-AT. [http://www.ntt-at.com/product/x-ray\\_chart/](http://www.ntt-at.com/product/x-ray_chart/). Accessed 23 Nov 2016

- [21] Huang XJ, Conley R, Bouet N, Zhou J, Macrander A, Maser J, Yan HF, Nazaretski E, Lauer K, Harder R, Robinson IK, Kalbfleisch S, Chu YS (2015) Achieving hard X-ray nanofocusing using a wedged multilayer Laue lens. *Opt Express* 23(10):12496–12507. doi:[10.1364/Oe.23.012496](https://doi.org/10.1364/Oe.23.012496)
- [22] Niese S, Krueger P, Kubec A, Braun S, Patommel J, Schroer CG, Leson A, Zschech E (2014) Full-field X-ray microscopy with crossed partial multilayer Laue lenses. *Opt Express* 22(17):20008–20013. doi:[10.1364/Oe.22.020008](https://doi.org/10.1364/Oe.22.020008)
- [23] Nazaretski E, Yan H, Lauer K, Huang X, Xu W, Kalbfleisch S, Yan H, Li L, Bouet N, Zhou J, Shu D, Conley R, Chu YS (2016) Nm-scale spatial resolution X-ray imaging with MLL nanofocusing optics: instrumental requirements and challenges. *AIP Conf Proc* 1764(1):040001. doi:[10.1063/1.4961143](https://doi.org/10.1063/1.4961143)
- [24] Nazaretski E, Xu W, Bouet N, Zhou J, Yan H, Huang X, Chu YS (2016) Development and characterization of monolithic multilayer Laue lens nanofocusing optics. *Appl Phys Lett* 108(26):261102. doi:[10.1063/1.4955022](https://doi.org/10.1063/1.4955022)
- [25] Als-Nielsen J, McMorrow D (2011) *Elements of modern X-ray physics*. Wiley, Hoboken
- [26] Born MAX, Wolf E (1980) CHAPTER V—geometrical theory of aberrations. In: *principles of optics* (sixth (corrected) edition). Pergamon, pp 203–232. doi:[10.1016/B978-0-08-026482-0.50012-8](https://doi.org/10.1016/B978-0-08-026482-0.50012-8)
- [27] Born MAX, Wolf E (1980) chapter VI—Image-FORMING INSTRUMENTS. In: *Principles of Optics* (sixth (corrected) edition). Pergamon, pp 233–255. doi: [10.1016/B978-0-08-026482-0.50013-X](https://doi.org/10.1016/B978-0-08-026482-0.50013-X)
- [28] Falch KV, Detlefs C, Di Michiel M, Snigireva I, Snigirev A, Mathiesen RH (2016) Correcting lateral chromatic aberrations in non-monochromatic X-ray microscopy. *Appl Phys Lett* 109(5):054103. doi:[10.1063/1.4960193](https://doi.org/10.1063/1.4960193)
- [29] Dimper RR, H.;Raimondi P, Ortiz LS; Sette F, Susini J (2015) ESRF upgrade programme phase II
- [30] Leemann SC, Andersson A, Eriksson M, Lindgren LJ, Wallen E, Bengtsson J, Streun A (2009) Beam dynamics and expected performance of Sweden's new storage-ring light source: MAX IV. *Phys Rev Spec Top-Ac* 12(12):120701. doi: [10.1103/PhysRevSTAB.12.120701](https://doi.org/10.1103/PhysRevSTAB.12.120701)
- [31] Donoghue PCJ, Bengtson S, Dong XP, Gostling NJ, Hultgren T, Cunningham JA, Yin C, Yue Z, Peng F, Stampanoni M (2006) Synchrotron X-ray tomographic microscopy of fossil embryos. *Nature* 442(7103):680–683. doi:[10.1038/nature04890](https://doi.org/10.1038/nature04890)
- [32] Weiss D, Schneider G, Niemann B, Guttman P, Rudolph D, Schmahl G (2000) Computed tomography of cryogenic biological specimens based on X-ray microscopic images. *Ultramicroscopy* 84(3–4):185–197. doi:[10.1016/S0304-3991\(00\)00034-6](https://doi.org/10.1016/S0304-3991(00)00034-6)
- [33] Zernike F (1942) Phase contrast, a new method for the microscopic observation of transparent objects. *Physica* 9(7):686–698. doi:[10.1016/S0031-8914\(42\)80035-X](https://doi.org/10.1016/S0031-8914(42)80035-X)
- [34] Snigirev A, Snigireva I, Kohn V, Kuznetsov S, Schelokov I (1995) On the possibilities of x-ray phase contrast microimaging by coherent high-energy synchrotron radiation. *Rev Sci Instrum* 66(12):5486–5492. doi:[10.1063/1.1146073](https://doi.org/10.1063/1.1146073)
- [35] Mokso R, Cloetens P, Maire E, Ludwig W, Buffiere JY (2007) Nanoscale zoom tomography with hard X rays using Kirkpatrick-Baez optics. *Appl Phys Lett* 90(14):144104. doi:[10.1063/1.2719653](https://doi.org/10.1063/1.2719653)
- [36] Cloetens P, Barrett R, Baruchel J, Guigay JP, Schlenker M (1996) Phase objects in synchrotron radiation hard X-ray imaging. *J Phys D Appl Phys* 29(1):133–146. doi:[10.1088/0022-3727/29/1/023](https://doi.org/10.1088/0022-3727/29/1/023)
- [37] Hegde S, Prabhu KN (2008) Modification of eutectic silicon in Al-Si alloys. *J Mater Sci* 43(9):3009–3027. doi:[10.1007/s10853-008-2505-5](https://doi.org/10.1007/s10853-008-2505-5)
- [38] Li JH, Albu M, Ludwig TH, Matsubara Y, Hofer F, Amberg L, Tsunekawa Y, Schumacher P (2014) Modification of eutectic Si in Al-Si based alloys. *Mater Sci Forum* 794–796:130–136. doi:[10.4028/www.scientific.net/MSF.794-796.130](https://doi.org/10.4028/www.scientific.net/MSF.794-796.130)
- [39] Ludwig TH, Li JH, Schaffer PL, Schumacher P, Amberg L (2015) Refinement of Eutectic Si in High Purity Al-5Si Alloys with Combined Ca and P Additions. *Metall Mater Trans A* 46(1):362–376. doi:[10.1007/s11661-014-2585-6](https://doi.org/10.1007/s11661-014-2585-6)
- [40] Li JH, Barrirero J, Engstler M, Aboufadel H, Mucklich F, Schumacher P (2015) Nucleation and Growth of Eutectic Si in Al-Si Alloys with Na Addition. *Metall Mater Trans A* 46(3):1300–1311. doi:[10.1007/s11661-014-2702-6](https://doi.org/10.1007/s11661-014-2702-6)
- [41] Barrirero J, Li JH, Engstler M, Ghafoor N, Schumacher P, Oden M, Mucklich F (2016) Cluster formation at the Si/liquid interface in Sr and Na modified Al-Si alloys. *Scripta Mater* 117:16–19. doi:[10.1016/j.scriptamat.2016.02.018](https://doi.org/10.1016/j.scriptamat.2016.02.018)
- [42] West R, Fredriksson H (1985) On the mechanism of faceted growth. *J Mater Sci* 20(3):1061–1068. doi:[10.1007/Bf00585750](https://doi.org/10.1007/Bf00585750)
- [43] Wang RY, Lu WH, Hogan LM (1999) Growth morphology of primary silicon in cast Al-Si alloys and the mechanism of concentric growth. *J Cryst Growth* 207(1–2):43–54. doi:[10.1016/S0022-0248\(99\)00347-4](https://doi.org/10.1016/S0022-0248(99)00347-4)
- [44] Mathiesen RH, Arnberg L, Li Y, Meier V, Schaffer PL, Snigireva I, Snigirev A, Dahle AK (2011) X-ray videomicroscopy studies of eutectic Al-Si solidification in Al-Si-Cu. *Metall Mater Trans A* 42(1):170–180. doi:[10.1007/s11661-010-0443-8](https://doi.org/10.1007/s11661-010-0443-8)
- [45] Jackson KA, Hunt JD (1966) Lamellar and rod eutectic growth. *T Metall Soc AIME* 236(8):1129–1142

- [46] Trivedi R, Magnin P, Kurz W (1987) Theory of eutectic growth under rapid solidification conditions. *Acta Metall* 35(4):971–980. doi:[10.1016/0001-6160\(87\)90176-3](https://doi.org/10.1016/0001-6160(87)90176-3)
- [47] Magnin P, Trivedi R (1991) Eutectic growth—a modification of the Jackson and Hunt theory. *Acta Metall Mater* 39(4):453–467. doi:[10.1016/0956-7151\(91\)90114-G](https://doi.org/10.1016/0956-7151(91)90114-G)
- [48] Karma A, Sarkissian A (1996) Morphological instabilities of lamellar eutectics. *Metall Mater Trans A* 27(3):635–656. doi:[10.1007/Bf02648952](https://doi.org/10.1007/Bf02648952)
- [49] Ginibre M, Akamatsu S, Faivre G (1997) Experimental determination of the stability diagram of a lamellar eutectic growth front. *Phys Rev E* 56(1):780–796. doi:[10.1103/PhysRevE.56.780](https://doi.org/10.1103/PhysRevE.56.780)
- [50] Akamatsu S, Bottin-Rousseau S, Faivre G (2004) Experimental evidence for a zigzag bifurcation in bulk lamellar eutectic growth. *Phys Rev Lett* 93(17):175701. doi:[10.1103/PhysRevLett.93.175701](https://doi.org/10.1103/PhysRevLett.93.175701)
- [51] Akamatsu S, Plapp M, Faivre G, Karma A (2004) Overstability of lamellar eutectic growth below the minimum-undercooling spacing. *Metall Mater Trans A* 35(6):1815–1828. doi:[10.1007/s11661-004-0090-z](https://doi.org/10.1007/s11661-004-0090-z)
- [52] Akamatsu S, Bottin-Rousseau S, Perrut M, Faivre G, Witusiewicz VT, Sturz L (2007) Real-time study of thin and bulk eutectic growth in succinonitrile-(D)camphor alloys. *J Cryst Growth* 299(2):418–428. doi:[10.1016/j.jcrysgro.2006.11.271](https://doi.org/10.1016/j.jcrysgro.2006.11.271)
- [53] De Wilde J, Froyen L, Witusiewicz VT, Hecht U (2005) Two-phase planar and regular lamellar coupled growth along the univariant eutectic reaction in ternary alloys: an analytical approach and application to the Al-Cu-Ag system. *J Appl Phys* 97(11):113515. doi:[10.1063/1.1906286](https://doi.org/10.1063/1.1906286)
- [54] Zimmermann G, Hecht U, Mathes M, Mathiesen RH (2010) Time resolved X-ray imaging of eutectic cellular patterns evolving during solidification of ternary Al-Cu-Ag alloys. *Int J Mater Res* 101(12):1484–1488. doi:[10.3139/146.110435](https://doi.org/10.3139/146.110435)
- [55] Park JM, Kim DH, Mattern N, Kim KB, Fleury E, Eckert J (2011) Microstructure and mechanical properties of Fe-Si-Ti-(Cu, Al) heterostructured ultrafine composites. *J Alloy Compd* 509:S367–S370. doi:[10.1016/j.jallcom.2010.10.112](https://doi.org/10.1016/j.jallcom.2010.10.112)
- [56] Kim TE, Park JM, Kuhn U, Eckert J, Kim WT, Kim DH (2012) In situ martensitic phase reinforced Fe-Nb-Ni-Mn ultrafine composite with enhanced mechanical properties. *Mat Sci Eng A-Struct* 531:51–54. doi:[10.1016/j.msea.2011.10.012](https://doi.org/10.1016/j.msea.2011.10.012)
- [57] Park JM, Kim TE, Sohn SW, Kim DH, Kim KB, Kim WT, Eckert J (2008) High strength Ni-Zr binary ultrafine eutectic-dendrite composite with large plastic deformability. *Appl Phys Lett* 93(3):031913. doi:[10.1063/1.2952755](https://doi.org/10.1063/1.2952755)
- [58] Tiwary CS, Mahapatra DR, Chattopadhyay K (2012) Effect of length scale on mechanical properties of Al-Cu eutectic alloy. *Appl Phys Lett* 101(17):171901. doi:[10.1063/1.4761944](https://doi.org/10.1063/1.4761944)
- [59] Narayanan T (2009) High brilliance small-angle X-ray scattering applied to soft matter. *Curr Opin Colloid Interface sc i* 14(6):409–415. doi:[10.1016/j.cocis.2009.05.005](https://doi.org/10.1016/j.cocis.2009.05.005)
- [60] Petoukhov MV, Svergun DI (2013) Applications of small-angle X-ray scattering to biomacromolecular solutions. *Int J Biochem Cell B* 45(2):429–437. doi:[10.1016/j.biocel.2012.10.017](https://doi.org/10.1016/j.biocel.2012.10.017)
- [61] Ozin GA, Yang SM (2001) The race for the photonic chip: colloidal crystal assembly in silicon wafers. *Adv Funct Mater* 11(2):95–104. doi:[10.1002/1616-3028\(200104\)11:2<95:Aid-Adfm95>3.0.Co;2-O](https://doi.org/10.1002/1616-3028(200104)11:2<95:Aid-Adfm95>3.0.Co;2-O)
- [62] You JX, Wang LL, Wang ZJ, Li JJ, Wang JC, Lin X, Huang WD (2016) Interfacial undercooling in solidification of colloidal suspensions: analyses with quantitative measurements. *Sci Rep-Uk* 6:28434. doi:[10.1038/srep28434](https://doi.org/10.1038/srep28434)
- [63] Schall P, Cohen I, Weitz DA, Spaepen F (2006) Visualizing dislocation nucleation by indenting colloidal crystals. *Nature* 440(7082):319–323. doi:[10.1038/nature04557](https://doi.org/10.1038/nature04557)
- [64] Schall P, Cohen I, Weitz DA, Spaepen F (2004) Visualization of dislocation dynamics in colloidal crystals. *Science* 305(5692):1944–1948. doi:[10.1126/science.1102186](https://doi.org/10.1126/science.1102186)
- [65] Thijssen JHJ, Petukhov AV, 'T Hart DC, Imhof A, van der Werf CHM, Schropp REI, van Blaaderen A (2006) Characterization of photonic colloidal single crystals by micro-radian X-ray diffraction. *Adv Mater* 18(13):1662–1666. doi:[10.1002/adma.200502732](https://doi.org/10.1002/adma.200502732)
- [66] Nho HW, Kalegowda Y, Shin HJ, Yoon TH (2016) Nanoscale characterization of local structures and defects in photonic crystals using synchrotron-based transmission soft X-ray microscopy. *Sci Rep UK*. doi:[10.1038/srep24488](https://doi.org/10.1038/srep24488)
- [67] Sitters G, Heller I, Broekmans OD, Farge G, Menges C, Wende W, Hell SW, Peterman EJG, Wuite GJ (2014) STED nanoscopy combined with optical tweezers reveals protein dynamics on densely covered DNA. *Opt Trapp Opt Micro-manip Xi*. doi:[10.1117/12.2062819](https://doi.org/10.1117/12.2062819)